

FastSurf: Fast Neural RGB-D Surface Reconstruction using Per-Frame Intrinsic Refinement and TSDF Fusion Prior Learning

Seunghwan Lee Gwanmo Park Hyewon Son Jiwon Ryu Han Joo Chae
ROKIT Healthcare, Inc.

{seunghwan.lee, gwanmo.park, hyewon.son, jiwon.ryu, hanjoo.chae}@rokit.co.kr

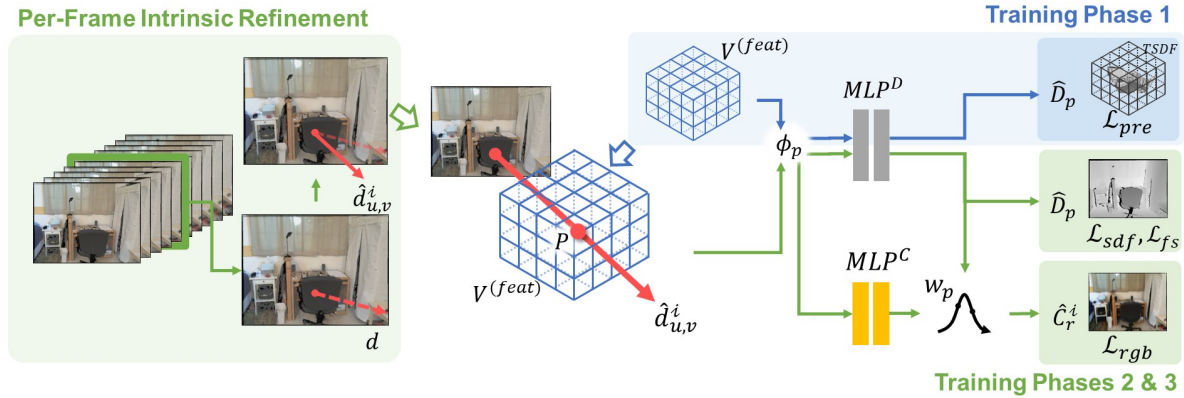


Figure 1: Our method proposes per-frame intrinsic refinement and classical TSDF Fusion [10] prior learning schemes for fast and high-quality 3D surface reconstruction. We adopt the Neural RGB-D method [2], revised with a hybrid representation through a dense feature grid and shallow MLPs. Our per-frame intrinsic refinement scheme compensates for the frame-specific distortion effects caused by the camera motion. The first phase of the training learns geometric prior using the TSDF Fusion algorithm and the later phases adopt a progressive learning technique [38].

Abstract

We introduce *FastSurf*, an accelerated neural radiance field (NeRF) framework that incorporates depth information for 3D reconstruction. A dense feature grid and shallow multi-layer perceptron are used for fast and accurate surface optimization of the entire scene. Our per-frame intrinsic refinement scheme corrects the frame-specific errors that cannot be handled by global optimization. Furthermore, *FastSurf* utilizes a classical real-time 3D surface reconstruction method, the truncated signed distance field (TSDF) Fusion, as prior knowledge to pretrain the feature grid to accelerate the training. The quantitative and qualitative experiments comparing the performances of *FastSurf* against prior work indicate that our method is capable of quickly and accurately reconstructing a scene with high-frequency details. We also demonstrate the effectiveness of our per-frame intrinsic refinement and TSDF Fusion prior learning techniques via an ablation study.

1. Introduction

Most modern mobile devices are now capable of capturing RGB-D images and videos without external sensors, and widely accessible RGB-D media expanded the use of 3D geometric information in various fields from augmented reality (AR) applications [5, 6, 16, 46] and 3D video streaming [41] to medical surgeries [7, 19, 48]. While fast and efficient classical 3D reconstruction methods [12, 27] based on the truncated signed distance field (TSDF) Fusion [10] were able to reflect surface geometry in real-time, inaccuracies in the reconstructed results due to the limitations of physical sensors hampered their use in the real-world applications where precision is critical. Recently, a neural RGB-D surface reconstruction method [2] incorporated a depth-measurement-based implicit surface representation into the volume rendering scheme of neural radiance field (NeRF) [24] and achieved high-quality geometry estimates of the entire scenes.

However, like most variants of NeRF, Neural RGB-

D [2] requires a long time to optimize for each newly given scene; the study reports to take 9 to 13 hours to optimize the networks depending on the size of the scene. While fast and precise 3D surface reconstruction is necessary for many real-world applications, methods proposed for quicker convergence of NeRF-style approaches mostly utilized the volume density representation focusing more on rendering unseen views rather than extracting 3D surface meshes [4, 25, 26, 38, 39, 49, 52], or sacrificed high-frequency details to achieve real-time speed [30, 37].

One of the most recent studies [42] that adopted a hybrid volume rendering scheme specifically for 3D surface reconstruction purposes showed impressive speed-up in convergence, but it was achieved at the cost of losing high-frequency details. Moreover, although some works [2] addressed the errors in camera poses and view-dependent color effects, the innate problems of the RGB-D video taken from the consumer-level cameras (*i.e.*, motion blur and rolling shutter problem) have not been considered.

In this work, we introduce *FastSurf*¹, an accelerated NeRF framework that incorporates depth information for 3D reconstruction. A dense feature grid and shallow multi-layer perceptron are used for fast and accurate surface reconstruction of the entire scene. Our per-frame intrinsic refinement scheme corrects the frame-specific errors that cannot be handled by global optimization. Specifically, four explicit representations (two for scaling and the other two for translation) are added when casting rays to handle the camera motion problems of RGB-D videos with a marginal effect on the training speed. Furthermore, *FastSurf* utilizes a classical real-time 3D surface reconstruction method, TSDF Fusion [10], as prior knowledge to pretrain the feature grid to give the model a head start when training. *FastSurf* consists of three optimization phases; it first leverages TSDF Fusion [10] to pretrain the feature grid and then learns low- and high-frequency implicit surfaces using coarse and fine feature grids, respectively. By comparing the performance against prior work (*i.e.*, Neural RGB-D [2] and *GO-Surf* [42]), we show how *FastSurf* quickly and accurately reconstructs a scene with high-frequency details. Moreover, we demonstrate the effectiveness of the TSDF Fusion prior learning and per-frame intrinsic refinement techniques via an ablation study.

2. Related work

Our method reconstructs 3D scene representation from a sequence of RGB-D video frames. It relates to the previous works on TSDF Fusion-based multi-view 3D reconstruction [10, 12, 27], coordinate-based implicit neural representations [2, 24, 29, 30, 37, 43, 47], and optimization speedup techniques for the neural models [25, 38, 42].

¹<https://rokit-healthcare.github.io/FastSurf>

2.1. Classical 3D reconstruction

A wide range of methods was researched for multi-view 3D geometry reconstruction including stereo matching and SLAM-based techniques [14, 15, 17, 18, 34, 35, 36, 50].

When reconstructing 3D surfaces from depth images, variations of TSDF Fusion have been the most commonly used method [53], where the surfaces were implicitly represented through TSDF in a uniform 3D grid [10]. Various improvements to the method have been implemented over the years including real-time application [27], efficient memory usage via spatial hashing [28], and better reconstruction quality through camera pose estimation [12].

While the methods based on TSDF Fusion were fast and efficient, they had clear limitations, often exhibiting holes or geometric artifacts in the reconstruction results. Nevertheless, we found that using TSDF Fusion output as the target while pretraining our voxel feature grid and MLPs accelerates the convergence and improves the overall optimization time as well as the reconstruction quality.

2.2. Neural radiance field and depth

Ever since Mildenhall *et al.* proposed NeRF [24], various attempts at adapting the neural radiance field representation and the volume rendering scheme to the depth images have been made. Some incorporated depth priors for better novel view synthesis [8, 13, 26, 44], while others used implicit neural representations for 3D surface reconstruction [9, 29, 30, 32, 37, 43, 47].

Among the methods for 3D reconstruction from RGB-D images, using a hybrid representation with both TSDF and volumetric radiance fields to incorporate the signed distance values into the classical volume rendering scheme saw the most success. Neural RGB-D [2] used two separate MLP networks to reconstruct 3D scenes with great accuracy, demonstrating the effectiveness of mixing photometric and depth loss terms. It additionally utilized pose optimization and deformation field correction techniques to further improve the quality. However, it takes a long time (9 to 13 hours) to optimize the networks, making it impractical for any time-sensitive applications.

2.3. Fast neural radiance field

As the long optimization time has been the critical weakness of NeRF and its variants, numerous methods for quicker convergence have been proposed [4, 25, 26, 30, 37, 38, 39, 49, 52]. In particular, DVGO [38] used a learnable feature grid to reduce the size of MLP network and thus decrease the training time, and Instant-NGP [25] employed multi-resolution hash encoding table for more memory- and computationally-efficient approach.

For reconstructing 3D surfaces, iMAP [37] and iSDF [30] had shown that representing implicit surfaces through MLP could be done in real-time. However, they relied on

keyframe selection and active sampling, sacrificing much of the details. GO-Surf [42] combined a multi-resolution feature grid with a hybrid volume rendering scheme akin to Neural RGB-D for much faster optimization speed which took dozens of minutes while having decent accuracy. It additionally used a smoothness prior which helped with quick convergence at the cost of high-frequency details.

Taking a similar approach to GO-Surf, we incorporate a dense feature grid and shallow MLPs to focus on recovering high-frequency details while preserving the speedup. We additionally introduce a per-frame intrinsic refinement scheme to fix the previously uncaught errors and a TSDF Fusion-guided pretraining phase for faster optimization, outperforming GO-Surf as well as the more accurate Neural RGB-D in terms of both reconstruction speed and quality.

Concurrent work Voxurf [45] and Vox-Surf [21] are similar to our work in that they both used voxel-based implicit surface representation and SDF-incorporated volume rendering schemes to accelerate 3D reconstruction. However, they did not utilize rich surface information that can be obtained from the depth channel as they mainly focus on using only color information. In addition, our work is primarily different as it corrects the camera intrinsic matrices frame-by-frame and leverages the classical TSDF Fusion as prior knowledge.

3. Method

We propose a fast neural RGB-D surface reconstruction method using a dense feature grid and shallow MLPs, with per-frame intrinsic refinement and TSDF Fusion-guided pretraining schemes to obtain high-fidelity results without sacrificing the speed. Similar to the previous RGB-D surface reconstruction methods [2, 42], we leverage the depth and corresponding color information from RGB-D video frames $\nu = \{\nu_i \mid i \in \mathbb{N}, i \leq \#frames\}$ to optimize our coordinate-based networks. As depicted in Fig. 1, our explicit-implicit hybrid geometry representation optimizes the volumetric radiance field and implicit surface based on TSDF in a continuous region of interest. Our three-phase training process leverages the TSDF Fusion algorithm and the progressive learning technique for efficient optimization.

3.1. Hybrid geometry representation

We adopt a dense feature grid to explicitly learn local features in grid cells. This explicit representation lowers the computational complexity compared to an MLP, significantly reducing the training time. We dynamically build the feature grid per scene:

$$V^{(feat)} : (N_x \times N_y \times N_z) \mapsto \mathbb{R}^F, \quad (1)$$

where F is a fixed hyperparameter for feature vector length and N_x, N_y, N_z are the feature grid dimensions varied according to the scene size. We use the depth frames and the estimated camera poses to calculate the minimum bounding box size of the scene— L_x, L_y, L_z . With the grid cell size gs , each of N_x, N_y, N_z is set to $\lceil L_x/gs \rceil, \lceil L_y/gs \rceil, \lceil L_z/gs \rceil$ respectively. The feature vector $\phi_{\mathbf{p}}$ for a 3D point \mathbf{p} is simply the trilinear interpolation of the feature vectors of the nearest 8 grid vertices \mathbf{P}_{near} .

$$\phi_{\mathbf{p}} = \text{interp}[V^{(feat)}(\mathbf{P}_{near})] \in \mathbb{R}^F \quad (2)$$

With the dense grid representation efficiently encoding local geometric features, we use shallow MLPs to decode the features into view-dependant color $C_{\mathbf{p},\mathbf{d}}^i$ and truncated signed distance value $\widehat{D}_{\mathbf{p}}$ of a 3D point \mathbf{p} . In order to decode the view-dependant color information, positional-encoded ray direction \mathbf{d} as in [24] and view-dependent latent embedding vector ξ introduced in [2, 23] are concatenated with the feature vector before inputting to the color MLP. As described in Eqs. (3) and (4), two separate MLPs were used for color and signed distance value, respectively.

$$C_{\mathbf{p},\mathbf{d}}^i = \text{MLP}^C(\phi_{\mathbf{p}}, \Lambda(\mathbf{d}), \xi_i), \quad (3)$$

$$\widehat{D}_{\mathbf{p}} = \text{MLP}^D(\phi_{\mathbf{p}}), \quad (4)$$

where i is the frame number and Λ is the frequency positional encoding function.

The neural rendering process is designed in a similar way as in [2]. Given a known camera intrinsic matrix, the camera ray \mathbf{r} for an image pixel (u, v) is cast along its casting direction \mathbf{d} :

$$\mathbf{d}_{u,v} = \frac{\varrho_{u,v}}{|\varrho_{u,v}|} \quad (5)$$

$$\varrho_{u,v} = \begin{bmatrix} 1/f_x & 0 & -c_x/f_x \\ 0 & -1/f_y & c_y/f_y \\ 0 & 0 & -1 \end{bmatrix} \begin{bmatrix} u \\ v \\ 1 \end{bmatrix} \quad (6)$$

where f_x, f_y are focal lengths and (c_x, c_y) is the principal point. For a 3D point \mathbf{p} , its weight value $\omega_{\mathbf{p}}$ for rendering the color image is calculated from the signed distance value:

$$\omega_{\mathbf{p}} = \sigma\left(\frac{\widehat{D}_{\mathbf{p}}}{tr}\right) \cdot \sigma\left(-\frac{\widehat{D}_{\mathbf{p}}}{tr}\right), \quad (7)$$

where tr is the truncation distance and σ is the sigmoid function. Finally, the rendered color \widehat{C} for a ray \mathbf{r} with direction \mathbf{d} of the i^{th} frame is the weighted sum of the radiance values on the sampled points \mathbf{p} along the ray:

$$\widehat{C}_{\mathbf{r}}^i = \frac{1}{\sum \omega_{\mathbf{p}}} \sum \omega_{\mathbf{p}} C_{\mathbf{p},\mathbf{d}}^i \quad (8)$$

3.2. Per-frame intrinsic refinement

Often, the camera intrinsic matrix is assumed to be the same across all frames. However, unlike still images, video frames are vulnerable to camera motion, resulting in motion blurs or rolling shutter effects (Fig. 2). As these effects can be handled by transformations in the image-plane coordinate [3, 31, 33], FastSurf is designed to correct the camera intrinsic matrix, which effectively changes the scale and translation of the projected image plane. The level of distortion varies from frame to frame and thus, having learnable features that can quickly correct the distortion per frame is critical.

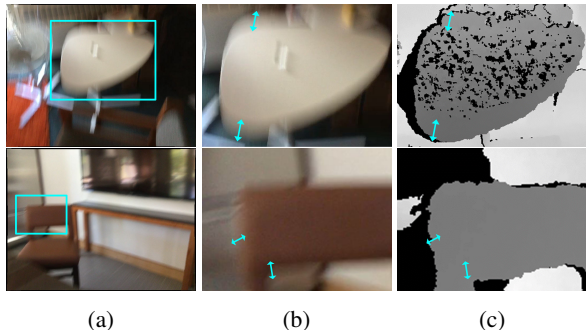


Figure 2: Samples from the ScanNet V2 [11] dataset demonstrate the negative impact of motion blurs [3] and rolling shutter effects [33]. The RGB frames (a, b) are blurry and distorted. The depth frames (c) likewise contain distorted object shapes.

Before handling this per-frame intrinsic refinement issue, we first adopt the image-plane deformation field and pose optimization techniques from [2] to correct the camera-pose errors and the potential global errors from the intrinsic parameters as well as the camera lens distortion. We modify the image-plane deformation field to use a two-layered shallow MLP to reduce the training time.

Our per-frame intrinsic refinement scheme is performed in between the image-plane deformation field and pose optimization to correct the frame-specific errors unhandled by the global optimizations. Specifically, we introduce four parameters per frame, two for scaling and the other two for translation purposes. Scaling and translation are applied to the normalized image coordinate before it is transformed into the world coordinate:

$$\hat{q}_{u,v}^i = \mathbf{s}^i \cdot (q_{u,v} + \tau^i) \quad (9)$$

$$\mathbf{s}^i = \begin{bmatrix} s_x^i & 0 & 0 \\ 0 & s_y^i & 0 \\ 0 & 0 & 1 \end{bmatrix}, \tau^i = \begin{bmatrix} \tau_x^i \\ \tau_y^i \\ 0 \end{bmatrix} \quad (10)$$

where s^i and τ^i are trainable parameters for i^{th} frame and optimized during the training. Accordingly, the refined cast-

ing direction $\hat{\mathbf{d}}$ is calculated from \hat{q} :

$$\hat{\mathbf{d}}_{u,v}^i = \frac{\hat{q}_{u,v}^i}{|\hat{q}_{u,v}^i|} \quad (11)$$

Eq. (11) replaces Eq. (5) for generating rays and sampling points. These parameters can be interpreted as correcting the principal point and focal lengths of the intrinsic matrix.

3.3. Optimization

FastSurf is optimized through a three-phase training process as depicted in Fig. 1. In the first phase, FastSurf quickly learns geometric prior using the classical real-time algorithm, TSDF Fusion [10]. Specifically, FastSurf builds a dense grid described in Eq. (1) with $F=1$ and runs TSDF Fusion with the identical scene and grid sizes. We randomly sample grid cells, query the center points, and compare them with the corresponding points from the results of TSDF Fusion using mean squared error:

$$\mathcal{L}_{pre} = \frac{1}{|\mathbf{P}_b|} \sum_{\mathbf{p} \in \mathbf{P}_b} (\hat{D}_{\mathbf{p}} - D_{\mathbf{p}}^f)^2, \quad (12)$$

where \mathbf{P}_b is the set of sampled center points and $D_{\mathbf{p}}^f$ is the signed distance value from the TSDF Fusion result. Only $V^{(feat)}$ and MLP^D are trained during this phase, while the other parameters are fixed at their initial values.

For the second and third phases, FastSurf adopts the progressive learning technique [38, 49] to successively learn low- and high-frequency details of the scene step by step. All the parameters including those that were fixed during the first phase are optimized during these phases.

During the second phase, FastSurf is trained with randomly sampled ray batch r_b from the input frames. Inspired by [2], we sample points S_c from the rays for every 15.625mm within the ray length where the ray length is varied depending on the scene, ranging from 4m to 10m, to cover the entire scene. Using the estimated signed distance values for each sampled point and the rendered color value as described in Eqs. (4) and (8), our loss function is defined similarly to [2]:

$$\mathcal{L} = \lambda_{fs} \mathcal{L}_{fs} + \lambda_{sdf} \mathcal{L}_{sdf} + \lambda_{rgb} \mathcal{L}_{rgb} + \lambda_{reg} \mathcal{L}_{reg} \quad (13)$$

\mathcal{L}_{fs} denotes the ‘free space’ loss that forces the sample points $\mathbf{p} \in S_{fs} \subset S_c$ that lie outside the truncated area to have the signed distance value of tr :

$$\mathcal{L}_{fs} = \frac{1}{|r_b|} \sum_{r \in r_b} \frac{1}{|S_{fs}|} \sum_{\mathbf{p} \in S_{fs}} (\hat{D}_{\mathbf{p}} - tr)^2 \quad (14)$$

\mathcal{L}_{sdf} compares the predicted signed distance value of the sample points $\mathbf{p} \in S_{sdf} \subset S_c$ lying within the truncated

area against D_r^i , the signed distance value observed in the depth frame:

$$\mathcal{L}_{sdf} = \frac{1}{|r_b|} \sum_{r \in r_b} \frac{1}{|S_{sdf}|} \sum_{\mathbf{p} \in S_{sdf}} (\widehat{D}_{\mathbf{p}} - D_r^i)^2 \quad (15)$$

\mathcal{L}_{rgb} measures the difference between the predicted rendered color of the rays and the observed color of the corresponding pixels:

$$\mathcal{L}_{rgb} = \frac{1}{|r_b|} \sum_{r \in r_b} (\widehat{C}_r^i - C_{u,v}^i)^2 \quad (16)$$

\mathcal{L}_{reg} is the regularization term and consists of three parts:

$$\begin{aligned} \mathcal{L}_{reg} &= \mathcal{R}_{\text{embed}} + \mathcal{R}_{\text{refine}} + \mathcal{R}_{\text{deform}}, \quad (17) \\ \mathcal{R}_{\text{embed}} &= \frac{1}{|\nu|} \sum_{\nu_i \in \nu} \xi_{\nu_i}^2, \\ \mathcal{R}_{\text{refine}} &= \frac{1}{|r_b|} \sum_{r \in r_b} ((s_r - 1)^2 + \tau_r^2), \\ \mathcal{R}_{\text{deform}} &= \frac{1}{|r_b|} \sum_{r \in r_b} w_{ipdf}^2 \end{aligned}$$

where w_{ipdf} are the weights for the image-plane deformation field network, and s_r and τ_r denote the transform parameters (Section 3.2) of the frame to which the ray r belongs.

FastSurf learns the fine details through the third phase, in which the dense feature grid is divided into higher resolutions so that the feature grid dimensions N_x, N_y, N_z become $\lceil L_x/(gs/2) \rceil, \lceil L_y/(gs/2) \rceil, \lceil L_z/(gs/2) \rceil$ respectively. We sample additional points S_f in small neighborhoods around the surfaces discovered from the previously sampled set of points S_c . The third phase is trained with the same loss function, Eq. (13), using both S_c and S_f .

3.4. Implementation details

We implemented our network with PyTorch, and the network was optimized using the ADAM optimizer [20] with 5×10^{-4} for learning rate, 0.9 for beta1, and 0.999 for beta2. The learning rate was set to exponentially decay so that it was decreased to a tenth for every 250K iterations. For the feature grid, we chose $F=12$ and $gs=10\text{cm}$. Its weights were initialized to 0. The signed distance values were truncated to $tr=5\text{cm}$. The MLP networks for the color and truncated signed distance values both consisted of 2 hidden layers with 128 nodes each. We conducted the positional encoding for the ray direction vector in 4 frequency levels. The MLP for the image-plane deformation field was built with 2 hidden layers with 64 nodes each. Per-frame intrinsic refinement optimization parameters were initialized to 1 for scaling and 0 for translation. Ray sampling number for S_f was set to 16. The λ weights for the loss terms

were set to 10 for λ_{fs} , 6×10^3 for λ_{sdf} , 0.5 for λ_{rgb} , and 0.1 for λ_{reg} . We ran 3K, 7K, and 65K iterations for each training phase, respectively. We used a CUDA implementation of the TSDF Fusion algorithm that can process, on average, 231.7 frames per second on Tesla V100 GPU [51]. The batch size of the grid cells in the first training phase was 1024. For the rest of the training phases, we sampled 768 to 2048 rays in a batch depending on the scene size.

4. Experiments

We demonstrate comparative studies of FastSurf against prior work. We designed a qualitative study on the real-scene dataset to prove that FastSurf outperforms its competitors in both the reconstruction quality and the training time. Quantitative evaluation was conducted using 10 synthetic scenes provided in [2] to show that our method achieves superior performance in comparative metrics. Finally, we conducted an ablation study to prove the effectiveness of the proposed framework components.

For the evaluation of each study, we extracted the truncated signed distance values in 1cm^3 resolution and ran MarchingCubes [22] algorithm to get the triangular meshes.

4.1. Datasets

We used ScanNet V2 [11] as a real-scene dataset during the qualitative study. ScanNet V2 contains RGB-D videos scanning 1,513 scenes from 707 unique indoor landscapes. Each scene was scanned using an iOS device externally attached with a Structure sensor. Since it used the rolling shutter method when capturing the images, ScanNet V2 often contains motion blur and other distortions as well as noisy depth measurements including holes and missing thin or transparent objects.

To compare quantitative results against the baselines, we used 10 synthetic scenes from [2]. They used indoor 3D models to photo-realistically render color and depth frames with ground truth camera trajectories. Depth frames were simulated with Kinect-like noises including holes and quantization noises.

4.2. Baselines

We compare our results with Neural RGB-D [2] and GO-Surf [42]. Specifically, we report our results at 20K and 75K iterations to respectively compare against GO-Surf and Neural RGB-D to show that FastSurf outperforms in terms of both efficiency and performance. We trained GO-Surf and Neural RGB-D with the hyperparameters recommended by the respective papers on a Tesla V100 GPU.

4.3. Results and discussion

Qualitative results The qualitative results are illustrated in Fig. 3. For the comparison with GO-Surf, our reconstruction results after 20K iterations—which took 11 to 15

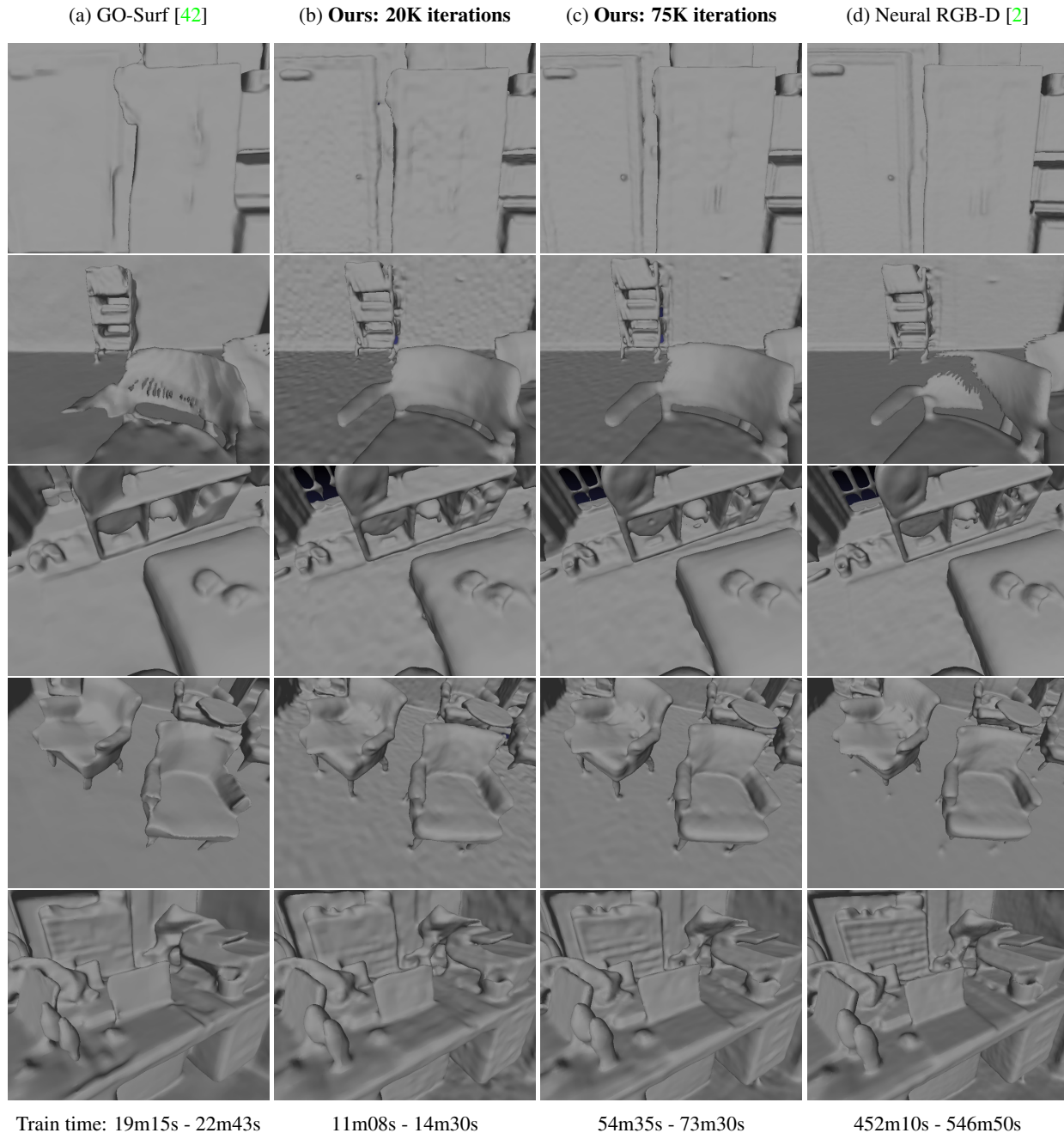


Figure 3: We compare our method with GO-Surf [42] and Neural RGB-D [2] at different points in time. The comparison was conducted using scenes 2, 5, 12, and 50 from ScanNet V2 [11]. When trained for a shorter amount of time, FastSurf-20K (b) recovers high-frequency details overlooked by GO-Surf (a) and generates much less erroneous surfaces. Given a longer training time, FastSurf-75K (c) achieves a quality on par with that of Neural RGB-D (d), but at a significantly shorter amount of time ($\times 7.7$ faster on average). It also fixes the errors caused by the camera motion.

minutes—is shown. The training time was less than that of GO-Surf (19-23 minutes) but FastSurf produced more fine details and fewer erroneous surfaces across the scenes. After 75K iterations, our reconstruction qualities showed

better results than Neural RGB-D, recovering the structures Neural RGB-D missed in some cases. Compared to Neural RGB-D, our training speed was 7.3 to 8.7 times faster.

Quantitative results We compared our method with baselines in terms of Chamfer ℓ_1 distance ($C-\ell_1$), intersection-over-union (IoU), normal consistency (NC), and F-score. In order to compute $C-\ell_1$, NC, and F-score, we sampled point clouds from the output meshes in 1cm^2 resolution. We used a threshold of 5cm for F-score. The evaluation meshes were voxelized with an edge length of 10cm to compute the IoU. As shown in Table 1, our result after 20K iterations outperforms GO-Surf in $C-\ell_1$, IoU, and F-score with less training time (21% faster on average). Our method took 94 minutes on average to train 75K iterations, which was 7.15 times faster than what Neural RGB-D took. At the same time, it showed superior $C-\ell_1$ and IoU scores and comparable F-score.

While FastSurf showed outstanding performance on the three major measures, it was less effective on the normal consistency, indicating that its results contained relatively uneven surfaces. The quantitative metrics imply that our method is best suited for quickly reconstructing complex geometries, rather than simple flat surfaces.

Ablation study The ablation study shows the effects of per-frame intrinsic refinement and TSDF Fusion-guided training phase. We compared results at the same iteration points without the per-frame intrinsic refinement or the first phase of training—TSDF Fusion prior learning (Fig. 4).

Our per-frame intrinsic refinement method fixes the erroneous parts of the objects. Although the pose correction scheme was used in both baselines and the refinement of camera parameters was used in Neural RGB-D, there still exists reconstruction errors in some cases. In addition to the image-plane deformation field which corrects the global parameters applied to all the frames simultaneously, our per-frame intrinsic refinement further corrects the frame-specific errors caused by camera motion. With only four additional parameters per frame, our scheme allowed these parameters to be optimized in the early stages of training, fixing the reconstruction errors in small iterations while increasing the training time by only 2.7% on average. Overall, the benefits of the per-frame intrinsic refinement outweigh the cost of the increased training time.

Method	$C-\ell_1 \downarrow$	IoU \uparrow	NC \uparrow	F-score \uparrow	Time
GO-Surf [42]	0.042	0.723	0.922	0.918	22m57s
Neural RGB-D [2]	0.052	0.757	0.922	0.938	669m59s
Ours (20K)	0.039	0.735	0.905	0.927	18m05s
Ours (75K)	0.041	0.768	0.914	0.938	93m45s

Table 1: Quantitative results on the synthetic scene dataset. FastSurf shows better $C-\ell_1$, IoU, and F-score than GO-Surf when trained for a shorter amount of time. After training for more iterations, it achieves better performances than Neural RGB-D with significantly less training time.

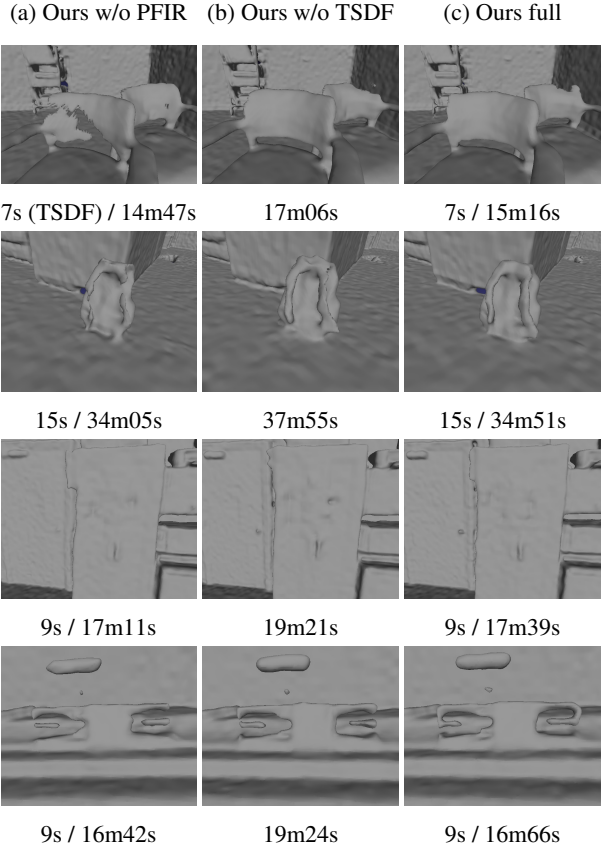


Figure 4: Ablation study. (a) Ours without per-frame intrinsic refinement (PFIR). (b) Ours without TSDF Fusion prior learning in the first phase of training (TSDF). (c) Ours with both methods applied. Timestamps below the subfigures represent the TSDF Fusion prior learning time (if applicable) and the total training time.

Fast classical algorithms are useful sources of information to utilize as prior knowledge of the scene despite their inaccuracies. The first phase of our training process that uses this prior knowledge is extremely fast as the signed distance values of 3D coordinates are directly learned instead of casting rays for the rendering process. Subsequent training phases refine the scene from this prior using the proposed optimization methods, correcting the inaccuracies from the classical algorithms and ultimately requiring less time to converge. As shown in Fig. 4, on all the scenes, the training time for the same iteration took several more minutes without the TSDF Fusion prior learning. TSDF Fusion prior learning phase also slightly improved the reconstruction quality of the objects. The benefits of utilizing the prior knowledge from TSDF Fusion can be maximized when fast optimization with a small number of training iterations is required.

4.4. Limitation

Our main limitation comes from the use of the dense feature grid that requires large amounts of memory and puts a limit to the available maximum scene size. For example, in the evaluation dataset, 1.3GB of memory was required for the scene size $18.0\text{m} \times 16.8\text{m} \times 12.3\text{m}$. However, despite the memory limitation, we leveraged the dense grid for efficient computation. It enabled us to use lightweight decoding MLPs and achieve 7.3 to 8.7 times faster convergence rate. Adopting other voxel representations introduced to handle the memory inefficiency [25,28,40] may decrease the memory usage without sacrificing the training speed or the performance.

Another limitation was the imbalance of ray density over the grid. A grid cell is involved in the training only if a ray from the batch passes through it. In other words, ray-abundant grid cells are prone to optimize better than ray-sparse cells. Depending on how the video was taken, some cells may never be learned in the training. In practice, one could scan more thoroughly around the regions of interest to ensure completeness. Setting different learning rates or loss weights as per ray density was also proposed in [38] which could be applicable to our method as well.

Finally, we use simple affine transformation matrices to correct the distortions from camera motion. While it proved to be effective at fixing errors without increasing the computational burden, more complex models were proposed to handle the motion blur or rolling shutter effects in the past [1,31,33]. Using more advanced or complicated modeling for the per-frame intrinsic refinement might be beneficial, but it could possibly trade off the speed with accuracy.

5. Conclusion

In this paper, we introduced FastSurf, an accelerated NeRF framework that incorporates depth information for 3D reconstruction. A dense feature grid and shallow MLPs were used for fast and accurate surface optimization of the entire scene. Our per-frame intrinsic refinement scheme corrects the frame-specific errors that cannot be handled by global optimization. Moreover, FastSurf utilized TSDF Fusion, a classical real-time 3D surface reconstruction method, as prior knowledge to pretrain the feature grid to accelerate the training. The quantitative and qualitative experiments compared the performances of FastSurf and prior work to show that our method is capable of quickly and accurately reconstructing a scene with high-frequency details. Specifically, FastSurf outperformed both GO-Surf [42] and Neural RGB-D [2] by 21% and 715% faster training time while having better reconstruction quality. We also demonstrated the effectiveness of the per-frame intrinsic refinement and TSDF Fusion prior learning techniques in the ablation study.

References

- [1] Cenek Albl, Zuzana Kukelova, Viktor Larsson, Michal Polic, Tomas Pajdla, and Konrad Schindler. From two rolling shutters to one global shutter. In *Proceedings of the IEEE/CVF Conference on Computer Vision and Pattern Recognition (CVPR)*, June 2020. 8
- [2] Dejan Azinović, Ricardo Martin-Brualla, Dan B Goldman, Matthias Nießner, and Justus Thies. Neural rgb-d surface reconstruction. In *Proceedings of the IEEE/CVF Conference on Computer Vision and Pattern Recognition (CVPR)*, pages 6290–6301, June 2022. 1, 2, 3, 4, 5, 6, 7, 8
- [3] Alastair Barber, Matthew Brown, Paul Hogbin, and Darren Cosker. Inferring changes in intrinsic parameters from motion blur. *Computers & Graphics*, 52:155–170, 2015. 4
- [4] Jonathan T. Barron, Ben Mildenhall, Matthew Tancik, Peter Hedman, Ricardo Martin-Brualla, and Pratul P. Srinivasan. Mip-nerf: A multiscale representation for anti-aliasing neural radiance fields, 2021. 2
- [5] Han Joo Chae, Youli Chang, Minji Kim, Gwanmo Park, and Jinwook Seo. Arphy: Managing photo collections using physical objects in ar. In *Extended Abstracts of the 2020 CHI Conference on Human Factors in Computing Systems*, pages 1–7, 2020. 1
- [6] Han Joo Chae, Jeong-in Hwang, and Jinwook Seo. Wall-based space manipulation technique for efficient placement of distant objects in augmented reality. In *Proceedings of the 31st Annual ACM Symposium on User Interface Software and Technology*, pages 45–52, 2018. 1
- [7] Han Joo Chae, Seunghwan Lee, Hyewon Son, Seungyeob Han, and Taebin Lim. Generating 3d bio-printable patches using wound segmentation and reconstruction to treat diabetic foot ulcers. In *Proceedings of the IEEE/CVF Conference on Computer Vision and Pattern Recognition (CVPR)*, pages 2539–2549, June 2022. 1
- [8] Anpei Chen, Zexiang Xu, Fuqiang Zhao, Xiaoshuai Zhang, Fanbo Xiang, Jingyi Yu, and Hao Su. Mvsnerf: Fast generalizable radiance field reconstruction from multi-view stereo, 2021. 2
- [9] Zhiqin Chen and Hao Zhang. Learning implicit fields for generative shape modeling, 2018. 2
- [10] Brian Curless and Marc Levoy. A volumetric method for building complex models from range images. In *Proceedings of the 23rd Annual Conference on Computer Graphics and Interactive Techniques, SIGGRAPH '96*, page 303–312, New York, NY, USA, 1996. Association for Computing Machinery. 1, 2, 4
- [11] Angela Dai, Angel X. Chang, Manolis Savva, Maciej Halber, Thomas Funkhouser, and Matthias Nießner. Scannet: Richly-annotated 3d reconstructions of indoor scenes. In *Proc. Computer Vision and Pattern Recognition (CVPR), IEEE*, 2017. 4, 5, 6
- [12] Angela Dai, Matthias Nießner, Michael Zollhöfer, Shahram Izadi, and Christian Theobalt. Bundlesfusion: Real-time globally consistent 3d reconstruction using on-the-fly surface re-integration, 2016. 1, 2

- [13] Kangle Deng, Andrew Liu, Jun-Yan Zhu, and Deva Ramanan. Depth-supervised nerf: Fewer views and faster training for free, 2021. [2](#)
- [14] Jakob Engel, Thomas Schöps, and Daniel Cremers. Lsdslam: Large-scale direct monocular slam. In David Fleet, Tomas Pajdla, Bernt Schiele, and Tinne Tuytelaars, editors, *Computer Vision – ECCV 2014*, pages 834–849, Cham, 2014. Springer International Publishing. [2](#)
- [15] Jakob Engel, Jürgen Sturm, and Daniel Cremers. Semi-dense visual odometry for a monocular camera. In *2013 IEEE International Conference on Computer Vision*, pages 1449–1456, 2013. [2](#)
- [16] Sarah Faltaous, Gabriel Haas, Liliana Barrios, Andreas Seiderer, Sebastian Felix Rauh, Han Joo Chae, Stefan Schneegass, and Florian Alt. Brainshare: A glimpse of social interaction for locked-in syndrome patients. In *Extended Abstracts of the 2019 CHI Conference on Human Factors in Computing Systems*, pages 1–6, 2019. [1](#)
- [17] Christian Forster, Matia Pizzoli, and Davide Scaramuzza. Svo: Fast semi-direct monocular visual odometry. In *2014 IEEE International Conference on Robotics and Automation (ICRA)*, pages 15–22, 2014. [2](#)
- [18] Michael Goesele, Noah Snavely, Brian Curless, Hugues Hoppe, and Steven Seitz. Multi-view stereo for community photo collections. pages 1–8, 11 2007. [2](#)
- [19] Hyunwoo Jo, Bo Young Choi, Giup Jang, Jung Pyo Lee, Ara Cho, Boyun Kim, Jeong Hwan Park, Jeonghwan Lee, Young Hoon Kim, and Jina Ryu. Three-dimensional bioprinted autologous omentum patch ameliorates unilateral ureteral obstruction-induced renal fibrosis. *Tissue Engineering Part C: Methods*, 28(12):672–682, 2022. [1](#)
- [20] Diederik P. Kingma and Jimmy Ba. Adam: A method for stochastic optimization. In Yoshua Bengio and Yann LeCun, editors, *3rd International Conference on Learning Representations, ICLR 2015, San Diego, CA, USA, May 7-9, 2015, Conference Track Proceedings*, 2015. [5](#)
- [21] Hai Li, Xingrui Yang, Hongjia Zhai, Yuqian Liu, Hujun Bao, and Guofeng Zhang. Vox-surf: Voxel-based implicit surface representation, 2022. [3](#)
- [22] William E. Lorensen and Harvey E. Cline. Marching cubes: A high resolution 3d surface construction algorithm. In *Proceedings of the 14th Annual Conference on Computer Graphics and Interactive Techniques, SIGGRAPH '87*, page 163–169, New York, NY, USA, 1987. Association for Computing Machinery. [5](#)
- [23] Ricardo Martin-Brualla, Noha Radwan, Mehdi S. M. Sajjadi, Jonathan T. Barron, Alexey Dosovitskiy, and Daniel Duckworth. Nerf in the wild: Neural radiance fields for unconstrained photo collections. In *Proceedings of the IEEE/CVF Conference on Computer Vision and Pattern Recognition (CVPR)*, pages 7210–7219, June 2021. [3](#)
- [24] Ben Mildenhall, Pratul P. Srinivasan, Matthew Tancik, Jonathan T. Barron, Ravi Ramamoorthi, and Ren Ng. Nerf: Representing scenes as neural radiance fields for view synthesis, 2020. [1](#), [2](#), [3](#)
- [25] Thomas Müller, Alex Evans, Christoph Schied, and Alexander Keller. Instant neural graphics primitives with a multiresolution hash encoding. *ACM Trans. Graph.*, 41(4):102:1–102:15, July 2022. [2](#), [8](#)
- [26] T. Neff, P. Stadlbauer, M. Parger, A. Kurz, J. H. Mueller, C. R. A. Chaitanya, A. Kaplanyan, and M. Steinberger. DONeRF: Towards real-time rendering of compact neural radiance fields using depth oracle networks. *Computer Graphics Forum*, 40(4):45–59, jul 2021. [2](#)
- [27] Richard A. Newcombe, Shahram Izadi, Otmar Hilliges, David Molyneaux, David Kim, Andrew J. Davison, Pushmeet Kohi, Jamie Shotton, Steve Hodges, and Andrew Fitzgibbon. Kinectfusion: Real-time dense surface mapping and tracking. In *2011 10th IEEE International Symposium on Mixed and Augmented Reality*, pages 127–136, 2011. [1](#), [2](#)
- [28] Matthias Nießner, Michael Zollhöfer, Shahram Izadi, and Marc Stamminger. Real-time 3d reconstruction at scale using voxel hashing. *ACM Trans. Graph.*, 32(6), nov 2013. [2](#), [8](#)
- [29] Michael Oechsle, Songyou Peng, and Andreas Geiger. Unisurf: Unifying neural implicit surfaces and radiance fields for multi-view reconstruction, 2021. [2](#)
- [30] Joseph Ortiz, Alexander Clegg, Jing Dong, Edgar Sucar, David Novotny, Michael Zollhoefer, and Mustafa Mukadam. isdf: Real-time neural signed distance fields for robot perception, 2022. [2](#)
- [31] Chandramouli Paramanand and Ambasamudram N. Rajagopalan. Non-uniform motion deblurring for bilayer scenes. In *2013 IEEE Conference on Computer Vision and Pattern Recognition*, pages 1115–1122, 2013. [4](#), [8](#)
- [32] Songyou Peng, Michael Niemeyer, Lars Mescheder, Marc Pollefeys, and Andreas Geiger. Convolutional occupancy networks, 2020. [2](#)
- [33] Vijay Rengarajan, Yogesh Balaji, and A. N. Rajagopalan. Unrolling the shutter: Cnn to correct motion distortions. In *2017 IEEE Conference on Computer Vision and Pattern Recognition (CVPR)*, pages 2345–2353, 2017. [4](#), [8](#)
- [34] Nikolay Savinov, Christian Häne, L’ubor Ladický, and Marc Pollefeys. Semantic 3d reconstruction with continuous regularization and ray potentials using a visibility consistency constraint. In *2016 IEEE Conference on Computer Vision and Pattern Recognition (CVPR)*, pages 5460–5469, 2016. [2](#)
- [35] D. Scharstein, R. Szeliski, and R. Zabih. A taxonomy and evaluation of dense two-frame stereo correspondence algorithms. In *Proceedings IEEE Workshop on Stereo and Multi-Baseline Vision (SMBV 2001)*, pages 131–140, 2001. [2](#)
- [36] Johannes L. Schönberger and Jan-Michael Frahm. Structure-from-motion revisited. In *2016 IEEE Conference on Computer Vision and Pattern Recognition (CVPR)*, pages 4104–4113, 2016. [2](#)
- [37] Edgar Sucar, Shikun Liu, Joseph Ortiz, and Andrew J. Davison. imap: Implicit mapping and positioning in real-time, 2021. [2](#)
- [38] Cheng Sun, Min Sun, and Hwann-Tzong Chen. Direct voxel grid optimization: Super-fast convergence for radiance fields reconstruction, 2021. [1](#), [2](#), [4](#), [8](#)
- [39] Towaki Takikawa, Joey Litalien, Kangxue Yin, Karsten Kreis, Charles Loop, Derek Nowrouzezahrai, Alec Jacobson,

- Morgan McGuire, and Sanja Fidler. Neural geometric level of detail: Real-time rendering with implicit 3d shapes, 2021. [2](#)
- [40] Towaki Takikawa, Joey Litalien, Kangxue Yin, Karsten Kreis, Charles Loop, Derek Nowrouzezahrai, Alec Jacobson, Morgan McGuire, and Sanja Fidler. Neural geometric level of detail: Real-time rendering with implicit 3d shapes. In *Proceedings of the IEEE/CVF Conference on Computer Vision and Pattern Recognition (CVPR)*, pages 11358–11367, June 2021. [8](#)
- [41] Telegie. <https://telegie.com/>, 2023. Accessed: 2023-02-17. [1](#)
- [42] Jingwen Wang, Tymoteusz Bleja, and Lourdes Agapito. Go-surf: Neural feature grid optimization for fast, high-fidelity rgb-d surface reconstruction, 2022. [2](#), [3](#), [5](#), [6](#), [7](#), [8](#)
- [43] Peng Wang, Lingjie Liu, Yuan Liu, Christian Theobalt, Taku Komura, and Wenping Wang. Neus: Learning neural implicit surfaces by volume rendering for multi-view reconstruction, 2021. [2](#)
- [44] Yi Wei, Shaohui Liu, Yongming Rao, Wang Zhao, Jiwen Lu, and Jie Zhou. Nerfingmvs: Guided optimization of neural radiance fields for indoor multi-view stereo, 2021. [2](#)
- [45] Tong Wu, Jiaqi Wang, Xingang Pan, Xudong Xu, Christian Theobalt, Ziwei Liu, and Dahua Lin. Voxurf: Voxel-based efficient and accurate neural surface reconstruction, 2022. [3](#)
- [46] Jianghao Xiong, En-Lin Hsiang, Ziqian He, Tao Zhan, and Shin-Tson Wu. Augmented reality and virtual reality displays: emerging technologies and future perspectives. *Light: Science & Applications*, 10(1):216, Oct 2021. [1](#)
- [47] Lior Yariv, Yoni Kasten, Dror Moran, Meirav Galun, Matan Atzmon, Ronen Basri, and Yaron Lipman. Multiview neural surface reconstruction by disentangling geometry and appearance, 2020. [2](#)
- [48] Ahmet Ç Yastı, Ali E Akgun, Aziz A Surel, Jeehee Kim, and Merve Akin. Graft of 3d bioprinted autologous minimally manipulated homologous adipose tissue for the treatment of diabetic foot ulcer. *Wounds: a Compendium of Clinical Research and Practice*, 35(1):E22–E28, 2023. [1](#)
- [49] Alex Yu, Sara Fridovich-Keil, Matthew Tancik, Qinhong Chen, Benjamin Recht, and Angjoo Kanazawa. Plenoxels: Radiance fields without neural networks, 2021. [2](#), [4](#)
- [50] Christopher Zach, Thomas Pock, and Horst Bischof. A globally optimal algorithm for robust tv-l1 range image integration. In *2007 IEEE 11th International Conference on Computer Vision*, pages 1–8, 2007. [2](#)
- [51] Andy Zeng, Shuran Song, Matthias Nießner, Matthew Fisher, Jianxiong Xiao, and Thomas Funkhouser. 3dmatch: Learning local geometric descriptors from rgb-d reconstructions. In *CVPR*, 2017. [5](#)
- [52] Xiaoshuai Zhang, Sai Bi, Kalyan Sunkavalli, Hao Su, and Zexiang Xu. Nerfusion: Fusing radiance fields for large-scale scene reconstruction, 2022. [2](#)
- [53] Michael Zollhöfer, Patrick Stotko, Andreas Görlitz, Christian Theobalt, Matthias Nießner, Reinhard Klein, and Andreas Kolb. State of the art on 3d reconstruction with rgb-d cameras. *Computer Graphics Forum*, 37:625–652, 05 2018. [2](#)